Insights into convective momentum transport and its parametrisation from idealised simulations of organised convection

Rachel L. Badlan [a]*, Todd P. Lane [a], Mitchell W. Moncrieff [b] and Christian Jakob [c]

[a] *ARC Centre of Excellence at The School of Earth Sciences, The University of Melbourne, Melbourne, Victoria, Australia*
[b] *NCAR, Boulder, USA*
[c] *ARC Centre of Excellence at The School of Mathematical Sciences, Monash University, Melbourne, Victoria, Australia*

*Correspondence to: The School of Earth Sciences, The University of Melbourne, Melbourne, VIC 3010, Australia. E-mail: rachel.badlan@unimelb.edu.au

Deep convection is an important process that influences the budgets of heat, moisture and momentum. In global models the thermodynamic effects of convection are normally treated through the convection parametrisation, with a separate formulation governing the convective momentum transport (CMT). CMT is composed of multiscale dynamical processes, including convective-scale CMT associated with updrafts and downdrafts, and mesoscale CMT associated with the quasi-steady circulation of organised systems. Like most convection parametrisations, current CMT parametrisations only represent convective-scale processes through relatively simple plume models. Thus, they do not fully represent the transports associated with organised systems, even though the tilted circulation associated with organised convection is a fundamental aspect of CMT. In addition, current schemes make simplifying assumptions about the interactions between convective updrafts and the mean flow - these assumptions are poorly constrained and are likely not good general representations of the processes at play.

This study revisits the problem of CMT, by examining the CMT budgets of simulated idealised mesoscale convective systems, including their sensitivity to horizontal resolution, domain size, and the boundary conditions. It is found that even for relatively large domains, horizontal gradient terms are still important, including the mesoscale pressure gradients which are normally neglected in CMT parametrisations. On the other hand, small domain calculations suppress organisation through artificially large compensating subsidence and hence provide unrealistic representations of the CMT evolution. Finally, examination of the cross-updraft/downdraft pressure gradients demonstrates significant uncertainties in their representation in current parametrisation schemes.

Key Words: convective momentum transport, mesoscale convective systems, parametrisation, Reynolds stress

Received . . .

1. Introduction

Deep convection is a globally important process that redistributes heat, moisture and momentum vertically throughout the troposphere. Convective momentum transport (CMT) is known to have a considerable effect on the both the zonal and meridional mean flow (Zhang and McFarlane (1995)). Earlier studies have shown it contributes to the Hadley circulation (Schneider (1975), Helfand (1979)), with Houze (1973) noting that CMT can have a similar magnitude to the rest of the terms comprising the atmospheric angular momentum budget. CMT is normally parametrised in global models, but uncertainties remain about the dynamics of CMT, its effects, and its representation in current schemes. This study revisits the problem of CMT using idealised simulations to assess some of the assumptions underlying its parametrisation.

CMT occurs on multiple scales, both temporally and spatially. Convective-scale transports are caused by unorganised convection, or the convective updrafts embedded within organised systems. The archetypal model described by Moncrieff (1992) demonstrates how the sign of mesoscale momentum transports are inherently linked to the tilt of the mesoscale convective system (MCS). His Fig. 10 shows how a positively tilted circulation produces correlated u' and w' terms resulting in positive CMT, and how a negatively tilted circulation produces anti-correlated terms, resulting in a negative CMT. These mesoscale fluxes can influence the larger-scale flow, with this process potentially feeding back on the convection itself (i.e. Moncrieff (1981), Flatau and Stevens (1987), Mechem et al. (2006), Mahoney et al. (2009)) and contributing to the formation of a variety of convective regimes (Lane and Moncrieff (2010)). LeMone (1983) studied the effect

of momentum transports across and along convective lines and found that organised convection can transport zonal momentum either upgradient or downgradient, thereby enhancing or reducing the vertical wind shear accordingly. Thus, CMT can defy 'mixing-length' theory (i.e., the representation of CMT as a diffusion process) in cases with countergradient transport. Depending on its characteristics, CMT can either strengthen a convective system and increase its longevity, or diminish it. Rotunno et al. (1988) and Weisman and Rotunno (2004)) explain why a system changes from downshear tilted to upshear tilted as it transitions from its initial stages to a mature system, and it follows that the momentum transport can change from up- to downgradient throughout the lifecycle.

Convective-scale momentum transports have been parametrised based on entraining plume models (e.g. Kershaw and Gregory (1997)) using the convective mass flux from the convective parametrisation scheme and empirical relationships that relate the cross-updraft pressure gradient to the large-scale vertical wind shear. Application of CMT parametrisations to global models have shown demonstrable improvement in the large-scale circulations including surface winds and precipitation (Richter and Rasch (2008)). Tropical circulations such as the Hadley cell, ITCZ, MJO and ENSO (Zhang and McFarlane (1995), Mapes and Wu (2001), Wu et al. (2003), Miyakawa et al. (2012)) are also better represented when CMT is accounted for. For example, Han and Pan (2006) used the Wu and Yanai (1994) parametrisation scheme, which reduced the forecast track error of hurricane prediction and improved the intensity. Parametrisation of CMT within regional-scale models has also been shown to affect the motion of MCSs (Mahoney et al. (2009)). Further highlighting the importance of CMT, Moncrieff and Liu (2006) demonstrated that a regional numerical weather prediction (NWP) model without parametrised CMT formed mesoscale convective systems with erroneous tilts and resolved CMT of the wrong sign (when compared to a higher resolution convection-permitting model).

A few different approaches have been used to parametrise CMT. The scheme developed by Schneider and Lindzen (1976) was based upon the work by Ooyama (1971) using a mass-flux approach to cumulus parametrisation and the assumption that in-cloud horizontal momentum is conserved. However, this assumption is only valid if a negligible horizontal across-cloud pressure gradient is present. LeMone (1983) determined that across-cloud pressure gradients have an important role in influencing in-cloud wind speeds which, along with observational work by Shapiro and Stevens (1980) led to the inclusion of the effects of pressure gradients in the Flatau and Stevens (1987) parametrisation scheme. Zhang and Cho (1991) also included pressure gradients by employing a simple model of flow around a cloud. Gregory et al. (1997) include parametrised across-updraft and downdraft pressure gradients to determine in-cloud horizontal velocities; this parametrisation scheme defines the pressure gradient across the updrafts to be proportional to the mass flux and the vertical wind shear. This relationship introduces a 'tunable' parameter to the Gregory et al. (hereafter referred to as GKI) scheme, which has been examined by Grubišić and Moncrieff (2000) and will be considered later in this study. It is apparent that the representation of across-updraft and downdraft horizontal pressure gradients have emerged as one of the key uncertainties in the parametrisation of CMT. However, recent modelling work by Romps (2012) has questioned its importance for unorganised convection. This issue is revisited in section 3.4. Nevertheless, it is critical to note that all of the above parametrisation schemes use simple plume models to represent the convection and therefore are unable to fully represent the transports associated with organised circulations, viz. mesoscale momentum transports.

A number of authors have used explicit models of moist convection to study CMT (e.g., Grubišić and Moncrieff (2000), Gao et al. (1990), Gallus and Johnson (1992) and Yang and Houze (1996)) and the underlying dynamics. In our study we build on this previous work by using a variety of idealised simulations to test some of the assumptions inherent in the CMT parametrisation schemes. Specifically, a range of model domain sizes are used to assess the contributions of terms involving horizontal gradients, which are normally neglected in parametrisations. Their sensitivity to model resolution is also considered. The across-updraft and downdraft pressure gradients are examined in the context of the relationships used in the GKI parametrisation and to assess the relative contributions of the convective-scale transports to the domain-mean tendency. The remainder of the paper is ordered as follows: the numerical model and its configuration is described in section 2, along with the decomposition of the momentum budget. The results of the idealised simulations are presented and analysed in section 3. The paper is summarised in section 4.

2. Idealised model simulations

2.1. *Model description and configuration*

All simulations use the Weather Research and Forecasting Model (WRF) - Advanced Research core (ARW) version 3.3 (Skamarock et al. (2008)). WRF-ARW is a mesoscale modelling system, developed principally by the National Center for Atmospheric Research and is used for real-time and operational forecasting as well as research applications. The model uses the fully compressible Eulerian nonhydrostatic equations, which are solved on a finite-difference mesh with Arakawa C-grid staggering and formulated using a mass-based vertical coordinate (Laprise (1992)). In this study moist processes are treated explicitly (no cumulus parametrisation) and represented by the WRF single-moment 6-class microphysics (WSM6) scheme (Hong and Lim (2006)). The effects of subgrid turbulence are parametrised using a predictive 1.5-order turbulence kinetic energy closure. For this study Coriolis effects and other physical processes (viz. radiation, surface friction, surface fluxes) are neglected.

The height of the computational domain is 35 km and a 10 km Rayleigh damping layer is imposed to prevent gravity wave reflection from the upper boundary. Three computational domains are used: 100 km x 50 km (denoted small, Sm), 400 km x 200 km (denoted medium, Med) and 800 km x 400 km (denoted large, Lg). For each of these domain sizes, three different horizontal grid spacings were used to explore resolution sensitivities (500 m, 1 km and 3 km). There are 71 vertical levels with an approximate vertical grid spacing of 500 m for all domains. The timesteps are 3 s, 6 s and 12 s for 500 m, 1 km and 3 km gridlengths, respectively. All model simulations are run for a duration of 6 hours - the domain configurations are summarised in Table 1. All domain configurations are run for both open and cyclic boundary conditions, except the 50 km x 50 km (square, Sq) domain with 1 km horizontal grid spacing (Sq_1km) uses cyclic boundary conditions only.

The initial model thermodynamic environment for all simulations is defined using the Weisman and Klemp (1982) analytic sounding (Fig 1(b)-(c)). The initial wind profile is shown in Fig. 1(a) and contains constant vertical shear near the surface such that

$$U_0(z) = \begin{cases} 0, & z > h; \\ U_0 - \frac{U_0 z}{h}, & z \leq h. \end{cases} \quad (1)$$

where U_0 = -18.0 m s^{-1} and h = 3.25 km. This wind profile is used because previous studies have shown that this low-level linear

Table 1. Simulation domain configurations.

Model run	Domain size	$\Delta x, \Delta y$
Sq_1km	50 km x 50 km	1 km
Sm_500m	100 km x 50 km	500 m
Sm_1km	100 km x 50 km	1 km
Sm_3km	100 km x 50 km	3 km
Med_500m	400 km x 200 km	500 m
Med_1km	400 km x 200 km	1 km
Med_3km	400 km x 200 km	3 km
Lg_500m	800 km x 400 km	500 m
Lg_1km	800 km x 400 km	1 km
Lg_3km	800 km x 400 km	3 km

shear produces a strong, long-lived MCS (Thorpe et al. (1982), Weisman and Rotunno (2004)). The meridional wind component v is initially zero. Convection is initiated by a temperature perturbation ('warm bubble') of 3 K in the horizontal centre of the domain with a radius of 10 km and a height of 1.5 km. The mean wind profile is free to evolve with the simulation; an example evolution of the mean zonal wind u is shown in Fig. 1(a) (from Med_1km, See Table 1, with cyclic boundary conditions). This evolution represents the effect of the mean momentum tendency, which leads to an increase in surface u, a decrease in upper-level u and an eventual reduction in the low-level shear.

2.2. *Convective system*

The result of all simulations is a three-dimensional mesoscale convective system of the leading convective-line trailing-stratiform type (e.g. Houze et al. (1989), Parker and Johnson (2000)), though there are structural differences in spatial extent and strength between the convection in the various size and resolution domains. As an example, the evolution and mature structure of a simulated storm (Med_1km, see Table 1) is shown in Figs. 2 & 3. The system covers about 200 km and 100 km in both the x- and y-directions respectively (Fig. 3). The vertical cross-section of the zonal wind in Fig. 2(c) implies the triple-branch model from Moncrieff (1992) (his Fig. 1(b)) with front-to-rear ascending flow, an overturning updraft branch, and a descending mesoscale downdraft at the rear of the system. A stagnation point is present at the surface, near x=170 km, identifying the leading edge of the cold pool that helps maintain the system by triggering new convection. The red contours in Fig. 2(d) represent the area of greatest negative perturbation pressure, which indicates the position of the mesolow, located behind the updraft. This is reinforced by the presence of a region of higher pressure at the front of the system.

The mean wind profile has positive low-level wind shear (Fig. 1) and Fig. 2 demonstrates that the main convective region of the mature system is upshear-tilted. The simulated systems evolve in a similar way to that depicted by Weisman and Rotunno (2004), with the convective region being downshear-tilted in its earliest stages and becoming upright as the cold pool develops (Fig. 2(b)). This evolution will be considered later.

2.3. *The momentum budget*

The form of the x-component of the inviscid horizontal momentum equations in height coordinates are:

$$\frac{\partial u}{\partial t} + u\frac{\partial u}{\partial x} + v\frac{\partial u}{\partial y} + w\frac{\partial u}{\partial z} = -\frac{1}{\rho}\frac{\partial p}{\partial x}, \tag{2}$$

where, u, v and w are the three velocity components, p is pressure, ρ is density, and t is time. As WRF is a fully compressible numerical model, the mass continuity equation is:

$$\frac{\partial \rho}{\partial t} + \frac{\partial \rho u}{\partial x} + \frac{\partial \rho v}{\partial y} + \frac{\partial \rho w}{\partial z} = 0 \tag{3}$$

Each of the variables are separated into the temporally varying domain mean wind and corresponding perturbation. The variables are now decomposed as $u = \bar{u}(t) + u'$, $v = \bar{v}(t) + v'$, $w = \bar{w}(t) + w'$ and $p = \bar{p}(t) + p'$, where the overbar represents the domain average and the primes denote perturbations. For the zonal wind component this becomes:

$$\begin{aligned}\frac{\partial \bar{u}}{\partial t} + \frac{\partial u'}{\partial t} + \frac{\bar{u}}{\rho}\frac{\partial \rho}{\partial t} + \frac{u'}{\rho}\frac{\partial \rho}{\partial t} + \frac{1}{\rho}\frac{\partial \rho\bar{u}\bar{u}}{\partial x} + \frac{2}{\rho}\frac{\partial \rho\bar{u}u'}{\partial x} + \frac{1}{\rho}\frac{\partial \rho u'u'}{\partial x} + \\ \frac{1}{\rho}\frac{\partial \rho\bar{u}\bar{v}}{\partial y} + \frac{1}{\rho}\frac{\partial \rho\bar{u}v'}{\partial y} + \frac{1}{\rho}\frac{\partial \rho u'\bar{v}}{\partial y} + \frac{1}{\rho}\frac{\partial \rho u'v'}{\partial y} + \frac{1}{\rho}\frac{\partial \rho\bar{u}\bar{w}}{\partial z} + \\ \frac{1}{\rho}\frac{\partial \rho\bar{u}w'}{\partial z} + \frac{1}{\rho}\frac{\partial \rho u'\bar{w}}{\partial z} + \frac{1}{\rho}\frac{\partial \rho u'w'}{\partial z} = -\frac{1}{\rho}\frac{\partial p}{\partial x}\end{aligned} \tag{4}$$

Each term in the above equation is then averaged horizontally across the domain (i.e., Reynolds averaging). After rearranging, removing terms that are identically zero, assuming $\bar{v} = 0$, and neglecting a few small terms this becomes:

$$\begin{aligned}\frac{\partial \bar{u}}{\partial t} = -\frac{\bar{u}}{\rho}\frac{\partial \rho u'}{\partial x} - \bar{w}\frac{\partial \bar{u}}{\partial z} - \frac{1}{\rho}\frac{\partial \rho u'^2}{\partial x} \\ - \frac{1}{\rho}\frac{\partial \rho u'v'}{\partial y} - \frac{1}{\rho}\frac{\partial \rho u'w'}{\partial z} - \frac{1}{\rho}\frac{\partial p}{\partial x}\end{aligned} \tag{5}$$

where each term now represents a horizontal mean, and variables with overbars ($^-$) represent the domain-mean value of the variable at each height level. Note that overbars over complete terms are omitted for simplicity. Note that for this paper, the equations for v (the meridional wind component) is not considered as there is negligible mean tendency on v because the mean wind and shear are aligned with the x-direction.

For periodic lateral boundary conditions, the mean vertical velocity ($\bar{w}$) and all of the terms involving horizontal derivatives are exactly zero. Thus, this simplification of Eqn. 5 leads to the well-known result:

$$\frac{\partial \bar{u}}{\partial t} = -\frac{1}{\rho}\frac{\partial \rho u'w'}{\partial z} \tag{6}$$

This infers that, for periodic conditions, the total tendency imposed on the mean flow can be wholly represented by the momentum flux divergence term $\frac{1}{\rho}\frac{\partial \rho u'w'}{\partial z}$. This result forms the basis of all parametrisation schemes of CMT.

3. Results

To calculate the momentum budgets and tendencies, the model output was first interpolated from the WRF native mass-based coordinate system to height coordinates. This interpolation was necessary to close the momentum budget as written in Eq. 4. The sum of all the terms comprising the momentum budget (Eq. 5) along with the mean tendency of $\bar{u}$, were calculated for all simulations with the difference between the sum of the terms and the mean tendency defining a residual. Budgets were initially compared for calculations using model output every 3, 15, 30 and 60 minutes for the Med_1km_open simulation (not shown). As expected, the budgets with the 3-minute output showed the smallest residual compared to the other time resolutions; 15-minute data provided similar results, with a notable increase in the residual for 30- and 60-minute data. The small amount of added accuracy for the 3-minute output was not worth the considerably larger data storage, and 15-minute model output is used for all budgets found herein.

3.1. *Analysis of momentum budgets and tendencies*

In order to compare the domain-mean vertical flux of horizontal momentum with the other terms comprising the momentum budget (Eqn. 5), Fig. 4(a) shows all terms that contribute to the mean tendency for the open boundary conditions, medium domain. It is obvious that although the momentum flux ($\rho u'w'$) term dominates the other terms and accounts for the overall sign of the tendency across the domain in the upper-levels, there are other terms that significantly contribute to the tendency on the mean flow. The terms that are most important within the momentum budget are $\frac{1}{\rho}\frac{\partial \rho u'w'}{\partial z}$, $\frac{1}{\rho}\frac{\partial \rho u'u'}{\partial x}$ and $\frac{1}{\rho}\frac{\partial p}{\partial x}$. As stated, the sign of the total tendency (indicated by the solid red line) at upper levels is consistent with the divergence of the vertical flux of horizontal momentum but this is offset by $\frac{1}{\rho}\frac{\partial p}{\partial x}$ and $\frac{1}{\rho}\frac{\partial \rho u'u'}{\partial x}$, which essentially comprise the Bernoulli pressure term.

The sum of all the budget terms (Fig. 4(b) - red line) is very similar to the actual tendency, i.e., there is a very small residual. The largest residual is found near the tropopause at approximately 10.5 km altitude. This larger residual at these heights is related to transient behaviour, presumably linked to overshooting convective updrafts, because calculations with 3-minute data showed a smaller residual at those heights.

In the first two hours of the simulation the mean momentum flux and tendency is much smaller than at other times (and over the whole 6-hour simulation) (Fig. 4(c)). The tendency has opposite sign at early times near the tropopause compared to later times, but is very small (Fig. 4(d)). Fig. 2(b) shows a slight downshear tilt suggesting that any transports due to mesoscale organisation, albeit weak, are potentially offset by those from convective-scale transports as the domain-mean momentum flux is near zero.

The three dominant terms - $\frac{1}{\rho}\frac{\partial \rho u'w'}{\partial z}$, $\frac{1}{\rho}\frac{\partial \rho u'u'}{\partial x}$ and $\frac{1}{\rho}\frac{\partial p}{\partial x}$ are also averaged across the convective updrafts and downdrafts to determine the convective-scale behaviour and its contributions to the domain-mean momentum budgets. Here updrafts are defined as regions within cloud that have vertical velocity greater than 1 m s^{-1}, and downdrafts are regions within cloud with vertical velocity less than -1 m s^{-1}. Figure 5 shows how these small-scale contributions to the tendency change as the convective system evolves. During the initial stages (i.e. the first two hours), the pressure gradient across updrafts is positive, changing to negative at low levels during the later stages as the system becomes organised. This suggests the pressure gradient acts to accelerate the low level flow in the downshear direction in the early stages and in the upshear direction in the mature stages. At low-levels the magnitude of this term increases as the system develops. The pressure gradients across the downdrafts generally show a weaker tendency of the opposite sign to the updraft tendencies.

The total cross updraft/downdraft momentum flux $\rho u'w'$ divergence (Fig. 5(c)) increases in magnitude as the system matures. The tendency across the updrafts acts to increase the zonal flow below about 4 km and decrease the flow above 4 km, consistent with net negative momentum flux and downgradient transport. The momentum flux tendency associated with the updrafts is larger than that from the downdrafts, which is mostly confined below 4 km. This result is consistent with intense convective cores and evaporatively driven downdrafts, which act to partially offset the tendency from updrafts.

Weisman and Rotunno (2004) explain how mesoscale convective systems evolve from being downshear tilted to upshear tilted as the baroclinically generated vorticity from the cold pool begins to dominate the environmental shear at low-levels. This explanation is consistent with the evolution of the convective system herein, with (Fig. 2 (a)-(c)) showing the transition from downshear to upright to upshear tilted over about 3 hours. However, the tendency from the updraft/downdraft momentum flux divergence (Fig. 5(c)) does not undergo this transition and maintains its vertical structure throughout the evolution. The only significant change from the early stages to the mature stages is the change in the cross-updraft pressure gradient. Later in the storm evolution the upshear-tilted mesoscale circulations work in concert with the convective-scale transports.

An interesting point to note is that the $\frac{1}{\rho}\frac{\partial \rho u'^2}{\partial x}$ term (Fig. 5(b)) across up/downdrafts, reinforces the momentum flux term (i.e. strengthens the tendency) at low altitudes. In the domain mean, however, the low altitude tendency from this term is small, which suggests the domain-mean mesoscale contribution balances the convective-scale contribution. Moreover, the total up/downdraft contributions from the three dominant terms (Fig. 5(d)) are consistent in sign with the domain-mean contributions at low altitudes (< 4 km). However above this level, the sign is opposite to the domain-mean terms in Figure 4(a). This difference in sign above 4 km suggests that the mesoscale tendencies oppose and dominate the convective-scale tendencies above the background shear layer.

3.2. *Effect of domain size on momentum budget*

Figure 6 compares the momentum budgets for the medium and large domains. For the larger domain the mean tendencies are smaller, due to the larger averaging area. As expected, the horizontal derivatives becoming less important the farther the domain boundary is from the convective area and tending to zero with increasing domain size. For the large domain the $\frac{1}{\rho}\frac{\partial \rho u'^2}{\partial x}$ is negligible. However, an important feature of Fig. 6(c) is that even in the large domain, the domain-mean pressure gradient is still an important component of the momentum budget. The pressure gradient generally reduces the magnitude of the tendency caused by the momentum flux. This *mesoscale pressure gradient* is an influential component of the momentum budget, even on scales much larger than the convective system, and acts to maintain the organised mesoscale circulation. The relevance of this result is that current CMT parametrisation schemes neglect this mesoscale pressure gradient term and only attempt to represent the impact of the convective-scale pressure gradient term on the in-cloud velocities (an example is the GKI scheme).

The tendencies for the cyclic simulations, however, are comprised solely of the momentum flux divergence ($\frac{1}{\rho}\frac{\partial \rho u'w'}{\partial z}$), as is assumed for all parametrisation schemes. This is because the horizontal derivatives - $\frac{1}{\rho}\frac{\partial p}{\partial x}$ and $\frac{1}{\rho}\frac{\partial \rho u'^2}{\partial x}$ - are identically zero. Of interest is that for each domain size, the $\overline{u}$ tendency for the domains with open boundary conditions (Fig. 6 (left column)) are simular to those for cyclic boundary conditions (right column). This is perhaps not surprising for the large domain as the horizontal gradient terms are small (see discussion above). However, this result is not necessarily expected for the medium domain. In particular, for the open boundary conditions the tendency from the momentum flux is large in magnitude and offset by the horizontal gradient terms. For the cyclic boundary conditions the momentum flux tendency (which is equal to the total tendency) is much smaller, allowing the $\overline{u}$ tendency for each simulation to be very similar. It might be that the net effect of the cyclic boundary conditions (and stronger descent, see discussion later) is to reduce the strength of the convection and hence the momentum flux, with the agreement in $\overline{u}$ tendency being fortuitous.

3.3. *Resolution sensitivity*

The momentum budgets for the different horizontal resolutions are compared (Fig. 7) and it is evident that the resolution

does not greatly affect the relative contributions from the terms that comprise the momentum budgets. Most of the terms from Eqn. 5 contribute to the total tendency for the medium domain. The strength of the domain mean momentum flux and pressure gradient tendencies in the upper troposphere is largest for the 3km model (Fig.7(c)) compared to the finer grid spacing simulations. At lower altitudes the differences are smaller. This upper-level sensitivity is likely because there is less entrainment and mixing in the 3 km simulation and therefore there is greater vertical transport of horizontal momentum beyond the middle troposphere.

Direct comparison of the domain mean tendencies (Fig. 8(a)) show the largest differences above the low-level shear layer in regions where convective updrafts and mesoscale circulations are strong. The 3 km grid spacing simulation shows a region of positive tendency at about 12 km, which is likely related to enhanced overshooting updrafts. There is no clear convergence of the results in terms of the mean tendency.

For the convective-scale contributions to the tendency, viz. $\rho u' w'$ averaged across the up/downdrafts, the simulations do show convergence between the 1 km and 500 m grid spacing simulation (Fig. 8(b)). The 3 km shows enhanced convective-scale fluxes above about 7 km altitude, consistent with less entrainment and larger undiluted updrafts (see e.g., (Bryan et al. 2003)). This apparent convergence at the convective scales, but not the domain-mean tendency suggests that at least some of the resolution sensitivity arises from changes in the mesoscale circulations with resolution.

These results compare favourably to those of Weisman et al. (1997), who found a similar behaviour for 2 km and 4 km grid spacing, which produced slightly greater momentum flux when compared to the 1 km simulation. Overall, the fluxes compare well due to the coarser resolution model runs producing mature, upshear-tilted circulations. They imply that resolutions up to 12 km will produce mesoscale structures and therefore CMT need not be parametrised in such cases. However, those results are specifically focused on the mesoscale structure of squall lines and not the convective-scale structures as shown in Fig. 8(b). As discussed by Bryan et al. (2003), care should be taken not to use the model output from 1 km resolution simulations to represent a benchmark or control, as much finer resolution is needed, $\mathcal{O}$(100 m), to produce turbulent flows including entrainment.

Another interesting point to note is the opposite sign of the momentum flux of the updrafts below 4 km and the downdrafts above 4 km. Figure 8(b) shows that the momentum flux from the downdrafts is positive above this height, and the updrafts are negative. Referring back to Fig. 2 (bottom), the mesoscale momentum transport due to the FTR flow and the rear-inflow jet (RIJ) have the same sign of $\rho u' w'$ (negative), which is consistent with the dominant updraft flux at mid- and upper levels and the downdraft flux at low-levels. The low-level countergradient updraft flux and upper-level countergradient downdraft flux likely arise from circulations that are tilted in the opposite direction to the convective system; Fig. 2(c) suggests that these circulations are located ahead of the convective system in the region of forward-tilted mesoscale circulations.

3.4. *Effect of domain size on simulated convective systems*

The sensitivity of the momentum transport to the size of the domain was investigated earlier to determine whether the assumptions underlying typical momentum transport parametrisation scheme are justified. Therefore, is it appropriate to approximate the tendency by the momentum flux only (as represented by Eqn. 6)? Also, is it appropriate to use small domains to study CMT as they struggle to represent the mesoscale transports, which we have shown in the previous section to be important? This is particularly relevant as it has become common to use long-running (radiative-convective equilibrium (RCE)) simulations with periodic boundary conditions to examine the structure and impact of moist convection, including momentum transport.

To explore this sensitivity, Hovmöller diagrams of cloud mixing ratio during the six hours simulation for all domain sizes with periodic boundary conditions were used to demonstrate how the different domains allow for the development of convection. In order to provide a direct comparison between the domains, for analysis purposes the domains were *trimmed* to the same size. The large and medium domains were trimmed to 100 km width and the square domain (50 km x 50 km) was duplicated. The cyclic simulations were also beneficial for this analysis because for open boundary conditions with small domains the convective system moves out of the domain. The largest two domains (Fig. 9 (top)) show the convective systems are maintained throughout the 6-hour simulation and beyond, and show very similar horizontal and temporal structure. Figure 9 (bottom) show that the small and the square domains have lifespans of around 2-3 hours only, dissipating thereafter. It is instructive to explore why these systems decayed earlier than those in the larger domains.

To determine what is causing these short-lived systems and why the convection in these small domains is consequently suppressed, the mean downward vertical velocity for the same (trimmed) regions shown in Fig. 9 was calculated. Figure 10 shows that the smaller domains have much stronger downward velocities, which suppresses the convection within those domains by stabilising the environment. The reason for this is that for periodic boundary conditions the domain-mean vertical velocity must be zero, and for a given convective system the strength of this subsidence must be larger for a smaller domain. As shown here for this environment, once the domain gets too small (i.e. $\leq$ 100 km x 50 km), the longevity of the convective system is reduced and it is unable to maintain a long-lived organised system.

One alternate explanation for the differences in organisation in the different sized domains is that the structure (and tilt) of the convective systems are different in their early stages, which cause them to fail to organise in the smaller domains. To determine whether the convective-scale behaviour of the convective systems in the smaller domains are unduly affected by the domain size at the early stages of their lifecycle, the momentum flux, the pressure gradient and the $\frac{1}{\rho}\frac{\partial \rho u'^2}{\partial x}$ terms averaged across the up/downdrafts for the small, medium and large domains were calculated during the first 2 hours of each simulation. As Fig. 11 indicates there is very little difference between the profiles from the various size domains. This implies that all the domains produce convective systems that are similar in structure during the initial stages of the simulation. Therefore in the first two hours all simulations have convective systems with similar convective-scale behaviour, and the small domains produce an adequate representation of the convective scales. It is the smaller domains, with their stronger compensating subsidence, that inhibits the transition of the convection to organised systems that can be maintained beyond a few hours.

Some recent studies (e.g. Romps (2012)) studied CMT using small domains approximately the size of our square domain and ran simulations to RCE. One conclusion of Romps's study was that the horizontal pressure gradient is not particularly important for the parametrisation of convective momentum transport. The results here show, however, that the small domain can produce systems with a notable cross-updraft pressure gradient (Fig. 11(a)), but these systems cannot be maintained. It unlikely such a system would form spontaneously in an RCE simulation, which would instead be dominated by unorganised convection with weaker cross-updraft pressure gradients.

3.5. *Evaluation of the Gregory parametrisation scheme*

The GKI parametrisation scheme (Gregory et al. (1997)) is popularly used to parametrise CMT (with shallow and deep convection often parametrised separately (Stratton et al. (2009))). The GKI scheme was developed using results from Kershaw and Gregory (1997), which was used to estimate the momentum transports from various regimes of deep convection. Parametrised transports are determined using the mass-flux from the model's cumulus parametrisation scheme as well as a parametrisation of the effects of cross-updraft pressure gradients. A key aspect of this parametrisation is the assumption that the convective-scale pressure gradients (i.e., across the updrafts and downdrafts) are proportional to the product of the mass flux and the mean vertical wind shear, such that (for updrafts)

$$-\frac{\partial}{\partial x}\left(\frac{p'}{\rho}\right)\Big|_u \sim C_u M_u \frac{\partial \overline{u}}{\partial z} \tag{7}$$

where C_u is a constant, M_u is the mass flux across the updraft given by $\rho\overline{w'}^u$, where $\overline{()}^u$ represents the averages over the area covered by convective updrafts, and $\overline{u}$ is the domain mean background wind. This relation was determined by linear theory and assumes that a high pressure anomaly exists on the upshear side on an updraft (see Rotunno and Klemp (1982)), akin to a plume in shear flow.

Figure 12 examines the terms in Eq. 7 across the updrafts, throughout the duration of the simulation using the medium domain with open boundary conditions. The mass flux M_u (Fig. 12a) is strictly positive (by definition) and accordingly the $M_u \frac{\partial \overline{u}}{\partial z}$ term (Fig. 12 (b)) is positive within the shear layer ($<$ 4 km), though varies in magnitude with time. Above the shear layer this term is small. The convective-scale pressure gradient (Fig. 12(c)) changes with both time and height, evolving from being negative at early times to being positive within the shear layer later, while remaining negative further aloft. This pressure variation, is broadly consistent with Eq. 7 in the first two hours, i.e. with the pressure gradient force being directed downshear, but as the system develops the pressure gradient force in the shear layer is directed upshear. This reversal of the low-level across-updraft pressure gradient is likely related to the development of the mesolow behind the leading convective line, as described by LeMone (1983), and is inconsistent with Eq. 7. This mesolow is also evident in Fig. 2 (c), as indicated by the red contours.

The parameter C_u (Fig. 12(d)) (which is only shown here below 3.5 km as it is poorly defined further aloft) varies both in magnitude and sign. The time variation in the pressure gradient is mainly responsible for the fact that C_u is neither constant with height nor one-signed, contrary to an assigned fixed value. Moreover, C_u is only positive in the early stages of the system evolution before the system is organised. Grubišić and Moncrieff (2000) also found a variation of the value of C_u with height and though they found the GKI approximation to be accurate in the mid-levels, it lacked accuracy elsewhere. Grubišić and Moncrieff (2000) suggest that C_u should be a function of height z, as it varies between levels. The results presented here support this result, but further suggest that the GKI formulation is inadequate for organised systems.

Previously C_u, which is a tunable parameter, has been assigned various values depending on the model in which it is implemented. Values have ranged from 0.7 (Gregory et al. (1997) which is also used by UKMO (Stratton et al. (2009)) and an earlier version of NCAR's Community Access Model (CAM) 3.0 (Richter and Rasch (2008)); 0.55 (Zhang and Wu (2003)); and recently, 0.4 in CAM 5.1 (Neale et al. (2010)). Over the 6-hour model run shown in Fig. 12(d)) the average value of C_u equals approximately -0.3 within the shear layer, which is smaller (in magnitude) and of the opposite sign to all of the above values. In the first two hours of the simulation, however, C_u is approximately 0.5, which is consistent with the above values.

As noted by Neale et al. (2010), the magnitude of C_u (and correspondingly C_d) has an important control on the strength of parametrised convective momentum transport as the pressure gradient is a 'sink' term; as C increases the strength of the parametrised momentum transport decreases. However, as shown earlier (e.g., Fig. 5) the pressure gradient can actually act in concert with the up/down draft fluxes, such as at low-levels in the early stages of the evolution of the convective system. Ultimately, this pressure gradient evolves with the convective system and as shown for this organised system is poorly represented by Eq. 7. This poor representation is because Eq. 7 does not take into account the upshear directed pressure gradient associated with the elevated mesolow behind the leading edge of organised systems.

3.6. *Evaluation of the Moncrieff mesoscale momentum transport models*

The Moncrieff analytic models of organised moist convection are based on the conservation of mass, entropy, total energy, vorticity and horizontal momentum generation for inviscid steady flow in Lagrangian space (Moncrieff (1981)). These nonlinear models are approximately exact because the sole assumption is that the buoyancy is a separable function of the vertical velocity, which is valid for moist adiabatic motion. These models have been comprehensively evaluated by cloud-system resolving model simulation data and field-campaign measurements (e.g. Houze (2004), Houze (2014), Moncrieff (2010)). In particular, the two-dimensional analytic models are solutions of the elliptic integro-differential vorticity equation:

$$\nabla^2\psi = G(\psi) + \int_{z_0}^{z}\left(\frac{\partial F}{\partial \psi}\right)_{z'} dz' \tag{8}$$

where ψ is the streamfunction, G is the environmental shear and the integral is the vorticity generated by the horizontal gradient of buoyancy.

The far-field solution of Eq. 8 provides open lateral boundary conditions for the two-dimensional models. Analytic models of three-dimensional propagating squall lines (Moncrieff and Miller (1976)), and upshear/downshear propagating convective bands (Lane and Moncrieff (2015)/Moncrieff and Lane (2015)) are tractable only in the far-field. However, the Lagrangian formulation of the analytic models (see below for the two-dimensional models) enables the three-dimensional transports to be calculated from the far-field solutions.

The two-dimensional Moncrieff (1992) archetypal model (Fig. 13), the minimalist mesoscale system, is governed by the quotient of work done by the horizontal pressure gradient and the inflow kinetic energy, $E = \Delta p_s / \frac{1}{2}\rho U_s^2$, where Δp_s and U_s are the surface pressure change across the system and the surface inflow speed, respectively i.e., the ratio of the two terms of the Bernoulli pressure. With application to MCSs, squall lines, and density currents the archetypal models have a distinguished rearward-tilted circulation, and the mesoscale momentum transport has sign opposite to that of the propagation speed, e.g., momentum transport is negative when the propagation speed is positive, and vice versa.

The Lagrangian based two-dimensional analytic models enables the momentum transport to be derived from the far-field solutions of the vorticity equation. The two-dimensional archetypes is as follows. Referring to Fig. 13, the momentum transport is for the total relative flow (u_m, w_m). Define the difference operator $\Delta = [\,]_0^{L_m}$ and the horizontal averaging

operator $< >= \frac{1}{L_m}\int_0^{L_m}(\,)\,dx$. Integration of the steady Eulerian momentum equation in the x-direction

$$\frac{\partial}{\partial x}\left(u_m^2+\frac{p_m}{\rho}\right)+\frac{\partial}{\partial z}\left(u_m w_m\right)=0 \tag{9}$$

gives

$$\frac{\partial}{\partial z}\left\langle u_m w_m\right\rangle=-\frac{1}{L_m}\Delta\left[u_m^2+\frac{p_m}{\rho}\right]_0^{L_m} \tag{10}$$

In the above, u_m and w_m are normalised by U_s, and $\frac{p_m}{\rho}$ by U_s^2. The mesoscale momentum transport divergence is proportional to the cross-system change of dynamic pressure and the aspect ratio ($\frac{1}{L_m}$) is the constant of proportionality. Integration of Eq. 10 with $w_m=0$ at the horizontal lower boundary gives the mesoscale momentum transport at height z.

$$\left\langle u_m w_m\right\rangle=-\frac{1}{L_m}\int_0^z\Delta\left[u_m^2+\frac{p_m}{\rho}\right]_0^{z'}dz' \tag{11}$$

The w_m = 0 boundary condition at the horizontal upper boundary provides a powerful integral constraint on the mesoscale momentum transport. It follows that the dynamic pressure determines the momentum tendency

$$\int_0^1\Delta\left[u_m^2+\frac{p_m}{\rho}\right]_0^{L_m}dz=0 \tag{12}$$

i.e., the horizontal momentum is redistributed but the net-momentum generation is zero.

There are important distinctions between the mesoscale momentum transport based on the analytic models and the traditional eddy-based momentum transport, where an eddy is defined as a deviation from the horizontal mean (see Eq. 4). In other words, the eddy flux is replaced by the total mesoscale transport divergence i.e., eddy + mean components. Therefore, the mesoscale acceleration of the mean flow vertical profile is

$$\frac{\delta}{\delta t}\left\langle u_m\right\rangle=-\alpha_m\frac{\partial}{\partial z}\left\langle u_m w_m\right\rangle=\alpha_m\frac{1}{L_m}\left[u_m^2+\frac{p_m}{\rho}\right]_0^{L_m} \tag{13}$$

where α_m is an amplitude function or closure (Moncrieff (1992), Eq. 24). Moncrieff (1992); Fig. 12, showed that the momentum transport divergence for the archetypal model accelerates/decelerates the mean flow in the lower/upper troposphere, respectively.

The above formulae can be evaluated using the numerical simulations herein with open lateral boundary conditions. The terms in Eqn. 10 are represented in Fig. 14 for the medium domain.

An important structural characteristic of the archetypal models is that the rearward tilt of the mesoscale circulation means that the sign of the mesoscale transport is opposite to the propagation vector, e.g., a system propagating in the positive x-direction has negative momentum transport. The archetypal model is controlled by $E=\Delta p/\frac{1}{2}\rho U_s^2$, the ratio of the two components of dynamic pressure at the lower boundary. Figure 2 of Moncrieff (1992) shows the morphology of the relative flow for systems in the range $-8\leq E\leq\frac{8}{9}$. The lower and upper limits represent a system with no downdraft and no overturning updraft (strict propagation), respectively. Systems featuring deep downdrafts and deep overturning updrafts are associated with small absolute values of E. This structure pertains to the numerical simulations because Δp is small and U_s = -18 ms^{-1} so E is approximately zero. Vertical integration of Eq. 17 in Moncrieff (1992) gives the momentum transport for $E=0$ as

$$\left\langle u_m w_m\right\rangle=\frac{4}{3}\left(\frac{z}{h}\right)^3-2\left(\frac{z}{h}\right)^2 \tag{14}$$

for $0\leq z\leq h$, and provides values for $h\leq z\leq 1$ due to the symmetry of the profile. The archetypal model momentum transport profile shown in Fig. 15(a) resembles the transport calculated from the numerical simulation in Fig. 15(b). In dimensional units the minimum value of $< u_m, w_m >$ in the archetypal model is -13.6 m^{2}s^{-2}, using L_m = 200/12 = 16.7 and U_s= -18 ms^{-1}. This is in good agreement with -15.5 m^{2}s^{-2} for the simulation results (Fig. 15(b)).

4. Synthesis and Conclusion

This study on the momentum budget of idealised convective systems, focused on aspects relevant for the parametrisation of convective momentum transport. Specifically, there are important sensitivities of the simulated momentum budget to model domain size and resolution, as well as the contributions from convective-scale transports to the overall budgets.

Simulations with varied domain size revealed the key role of horizontal gradient terms in contributing to the momentum budget. In particular, even for relatively large domains (viz. the 'medium' domain that was 400 km long) the horizontal pressure gradient was a notable contributor to the mean flow tendency. This *mesoscale* pressure gradient arose entirely from the simulated convective system, acting to maintain the organised circulation associated with that system. This mesoscale pressure gradient mostly opposes the tendency from the convective momentum flux divergence, and for the 'medium' domain was about half the magnitude of the momentum flux tendency. Even for the 'large' domain (length = 800 km), the mesoscale pressure gradient was about one quarter the magnitude of the momentum flux term. This specific result has important implications for CMT parametrisation as these domain sizes are larger than most global model grid boxes; this mesoscale pressure gradient is not represented in any scheme, but it clearly plays an important role for mesoscale systems. Even when the work done by the static pressure ($\frac{p}{\rho}$) is identically zero; namely E=0, the system still has a distinguished vertical tilt (see Moncrieff (1992); Fig. 4) that provides mesoscale momentum transport.

The 'small' domain simulations considered here were not large enough for the convective systems to evolve and maintain themselves realistically. As shown in Fig. 11, the systems across all domains develop in a similar fashion for the first few hours. The pressure gradient and the structure of the convective system in these small domains are similar during the first two hours of the simulation (Fig. 5 and Fig. 9). However, when the domains are too small $\mathcal{O}(\leq$ 100 kms), then the convection is suppressed by overly strong subsidence and is unable to become properly organised. This has important implications for the interpretation of momentum fluxes associated with convection in small-domain RCE simulations e.g., Romps (2012), as they are unable to properly represent organisation.

The effect of model resolution on the CMT showed the 3 km grid spacing model producing larger fluxes and more convective overshoots than higher resolution domains. This result was consistent with previous studies that attribute some of the sensitivities to insufficient entrainment at these convection-permitting resolutions. Though, at least for those simulations

presented here, there seemed to be convergence of the convective-scale fluxes at grid spacings of 1 km.

Comparison of the convective-scale transports, i.e., those associated with individual updrafts and downdrafts, and those associated with the domain mean finds that in the early stages of evolution the convective-scales work against the mesoscales and result in a near-zero tendency. At mature stages, after the system tilts upshear, the convective-scale and mesoscale transports act in concert in a downgradient manner. As part of this evolution the low-level cross-draft pressure gradients change sign during the system evolution associated with the development of organised mesoscale circulations.

The most common parametrisations for convective momentum flux, which are based on the GKI scheme, use entraining plume models and incorporate a simple representation of the effects of the cross-updraft pressure gradient on the momentum tendency. As shown here, this representation poorly reproduces the evolution of the pressure gradient, as the assumed constant of proportionality between the pressure gradient and the product of the mean shear and the mass-flux actually changes sign. This difficulty arises due to the inability of such schemes to properly represent the processes associated with organised systems' notably vertical tilt. This underlines the importance of an improved representation of the roles of mesoscale transports in CMT parametrisations, which should differ in their formulation from downgradient-based representations of the transport properties of unorganised plumes.

Acknowledgements

This work is funded by the Australian Research Council (ARC) Centre of Excellence for Climate System Science (CE110001028). Computing facilities were provided by the Victorian Partnership for Advanced Computing (VPAC) and the National Computational Infrastructure facility (NCI). NCAR is sponsored by the National Science Foundation.

References

Bryan, G. H., J. C. Wyngaard, and J. M. Fritsch, 2003: Resolution requirements for the simulation of deep moist convection. *Mon. Wea. Rev.*, **131**, 2394–2416.

Flatau, M. and D. E. Stevens, 1987: The effect of horizontal pressure gradients on the momentum transport in tropical convective lines. Part I: The results of the convective parameterization. *J. Atmos. Sci.*, **44**(15), 2074–2087.

Gallus, W. A. and R. H. Johnson, 1992: The momentum budget of an intense midlatitude squall line. *J. Atmos. Sci.*, **49**(5), 422–450.

Gao, K., D.-L. Zhang, M. W. Moncrieff, and H.-R. Cho, 1990: Mesoscale momentum budget in a midlatitude squall line: A numerical case study. *Mon. Wea. Rev.*, **118**, 1011–1028.

Gregory, D., R. Kershaw, and P. Inness, 1997: Parameterization of momentum transport by convection. II: Tests in single-column and general circulation models. *Quart. J. Roy. Meteor. Soc.*, **123**, 1153–1183.

Grubišić, V. and M. W. Moncrieff, 2000: Parameterization of convective momentum transport in highly baroclinic conditions. *J. Atmos. Sci.*, **57**, 3035–3049.

Han, J. and H.-L. Pan, 2006: Sensitivity of hurricane intensity forecast to convective momentum transport parameterization. *Mon. Wea. Rev.*, **134**, 664–674.

Helfand, H. M., 1979: The effect of cumulus friction on the simulation of the January Hadley Circulation by the GLAS model of the general circulation. *J. Atmos. Sci.*, **36**, 1827–1843.

Hong, S.-Y. and J.-O. J. Lim, 2006: The WRF single-moment 6-class microphysics scheme (WSM6). *J. Kor. Meteor. Soc.*, **42**(2), 129–151.

Houze, R. A., 1973: A climatological study of vertical transports by cumulus-scale convection. *J. Atmos. Sci.*, **30**(6), 1112–1123.

Houze, R. A., 2004: Mesoscale convective systems. *Rev. Geophys.*, **42**, RG4003, doi:10.1029/2004RG000150.

Houze, R. A., 2014: *Cloud Dynamics*. Elsevier/Academic Press, Oxford, 432 pp., 2nd ed. edition.

Houze, R. A., S. A. Rutledge, M. I. Biggerstaff, and B. F. Smull, 1989: Interpretation of doppler weather radar displays of midlatitude mesoscale convective systems. *Bull. Amer. Meteor. Soc.*, **70**, 608–619.

Kershaw, R. and D. Gregory, 1997: Parameterization of momentum transport by convection. I: Theory and cloud modelling results. *Quart. J. Roy. Meteor. Soc.*, **123**(541), 1133–1151.

Lane, T. P. and M. W. Moncrieff, 2010: Characterization of momentum transport associated with organized moist convection and gravity waves. *J. Atmos. Sci.*, **67**, 3208–3225.

Lane, T. P. and M. W. Moncrieff, 2015: Long-lived mesoscale systems in a low-convective inhibition environment. Part I: Upshear propagation. *J. Atmos. Sci.*, **72**, 4297–4318.

Laprise, R., 1992: The Euler equations of motion with hydrostatic pressure as an independent variable. *Mon. Wea. Rev.*, **120**, 197–207.

LeMone, M., 1983: Momentum transport by a line of cumulonimbus. *J. Atmos. Sci.*, **40**, 1815–1834.

Mahoney, K. M., G. M. Lackmann, and M. D. Parker, 2009: The role of momentum transport in the motion of a quasi-idealized mesoscale convective system. *Mon. Wea. Rev.*, **137**, 3316–3338.

Mapes, B. E. and X. Wu, 2001: Convective eddy momentum tendencies in long cloud-resolving model simulations. *J. Atmos. Sci.*, **58**, 517–526.

Mechem, D. B., S. S. Chen, and R. A. Houze, 2006: Momentum transport processes in the stratiform regions of mesoscale convective systems over the western pacific warm pool. *Quart. J. Roy. Meteor. Soc.*, **132**, 709–736.

Miyakawa, T., Y. N. Takayabu, T. Nasuno, H. Miura, M. Satoh, and M. W. Moncrieff, 2012: Convective momentum transport by rainbands within a Madden-Julian oscillation in a global nonhydrostatic model with explicit deep convective processes. *J. Atmos. Sci.*, **69**, 1317–1338.

Moncrieff, M. W., 1981: A theory of organized steady convection and its transport properties. *Quart. J. Roy. Meteor. Soc.*, **107**, 29–50.

Moncrieff, M. W., 1992: Organized convective systems: Archetypal dynamical models, mass and momentum flux theory, and parametrization. *Quart. J. Roy. Meteor. Soc.*, **118**, 819–850.

Moncrieff, M. W., 2010: *Climate Dynamics: Why does climate vary?*, volume 189 of *Geophys. Monogr.* American Geophysical Union, 3-36.

Moncrieff, M. W. and T. P. Lane, 2015: Long-lived mesoscale systems in a low-convective inhibition environment. Part II: Downshear propagation. *J. Atmos. Sci.*, **72**, 4319–4336.

Moncrieff, M. W. and C. Liu, 2006: Representing convective organisation in prediction models by a hybrid strategy. *J. Atmos. Sci.*, **63**, 3404–3420.

Moncrieff, M. W. and M. J. Miller, 1976: The dynamics and simulation of tropical cumulonimbus and squall lines. *Quart. J. Roy. Meteor. Soc.*, **102**, 373–394.

Neale, R. B., C.-C. Chen, A. Gettekman, P. H. Lauritzen, S. Park, D. L. Williamson, A. J. Conley, R. Garcia, D. Kinnison, J.-F. Lamarque, D. Marsh, M. Mills, A. K. Smith, S. Tilmes, F. Vitt, H. Morrison, P. Cameron-Smith, W. D. Collins, M. J. Iacono, R. C. Easter, S. J. Ghan, X. Liu, P. J. Rasch, and M. A. Taylor, 2010: Description of the NCAR Community Atmosphere Model (CAM 5.0). Technical report, National Center for Atmospheric Research.

Ooyama, K., 1971: A theory on parameterization of cumulus convection. *J. Meteor. Soc. Japan*, **49**, 744–756.

Parker, M. D. and R. H. Johnson, 2000: Organizational modes of midlatitude mesoscale convective systems. *Mon. Wea. Rev.*, **128**, 3413–3436.

Richter, J. and P. Rasch, 2008: Effects of convective momentum transport on the atmospheric circulation in the Community Atmosphere Model, version 3. *J. Atmos. Sci.*, **21**, 1487–1499.

Romps, D. M., 2012: On the equivalence of two schemes for convective momentum transport. *J. Atmos. Sci.*, **69**, 3491–3500.

Rotunno, R., J. Klemp, and M. Weisman, 1988: A theory for strong, long-lived squall lines. *J. Atmos. Sci.*, **45**, 463–485.

Rotunno, R. and J. B. Klemp, 1982: The influence of the shear-induced pressure gradient on thunderstorm motion. *Mon. Wea. Rev.*, **110**, 136–151.

Schneider, E. K., 1975: *The Hadley circulation of the earth's atmosphere*. PhD thesis, Harvard Univ., Cambridge, Mass.

Schneider, E. K. and R. S. Lindzen, 1976: A discussion of the parameterization of momentum exchange by cumulus convection. *J. Geophys. Res.*, **81**(18), 3158–3160.

Shapiro, L. J. and D. E. Stevens, 1980: Parameterization of convective effects on the momentum and vorticity of synoptic-scale Atlantic tropical waves. *Mon. Wea. Rev.*, **108**, 1816–1826.

Skamarock, W., J. Klemp, J. Dudhia, D. Gill, D. Barker, M. Duda, X.-Y. Huang, and J. Powers, 2008: A description of the advanced research WRF Version 3. Technical report, NCAR.

Stratton, R. A., A. Stirling, and S. Derbyshire, 2009: Changes and development to convective momentum transport (CMT) parameterization based on analysis of CRM and SCM. Technical Report 530, Met Office.

Thorpe, A. J., M. J. Miller, and M. W. Moncrieff, 1982: Two-dimensional convection in non-constant shear: A model of mid-latitude squall lines. *Quart. J. Roy. Meteor. Soc.*, **108**, 739–762.

Weisman, M. and J. Klemp, 1982: The dependence on numerically simulated convective storms on vertical wind shear and buoyancy. *Mon. Wea. Rev.*, **110**, 504–520.

Weisman, M. and R. Rotunno, 2004: "A theory for strong, long-lived squall lines" revisited. *J. Atmos. Sci.*, **61**, 361–382.

Weisman, M. L., W. C. Skamarock, and J. B. Klemp, 1997: The resolution dependence of explicitly modeled convective systems. *Mon. Wea. Rev.*, **125**, 527–548.

Wu, X., X.-Z. Liang, and G. J. Zhang, 2003: Seasonal migration of the ITCZ precipitation across the equator: Why can't GCMs simulate it? *Geophys. Res. Lett.*, **30**, 1824–1828.

Wu, X. and M. Yanai, 1994: Effects of vertical wind shear on the cumulus transport of momentum: observations and parameterization. *J. Atmos. Sci.*, **51**(12), 1640–1660.

Yang, M.-J. and R. A. Houze, 1996: Momentum budget of a squall line with trailing stratiform precipitation: calculations with a high-resolution numerical model. *J. Atmos. Sci.*, **53**(23), 3629–3652.

Zhang, G. J. and H.-R. Cho, 1991: Parameterization of the vertical transport of momentum by cumulus clouds. part I: Theory. *J. Atmos. Sci.*, **48**(12), 1483–1492.

Zhang, G. J. and N. A. McFarlane, 1995: Role of convective scale momentum transport in climate simulation. *J. Geophys. Res.* 1417–1426.

Zhang, G. J. and X. Wu, 2003: Convective momentum transport and perturbation pressure field from a cloud-resolving model simulation. *J. Atmos. Sci.*, **60**, 1120–1139.

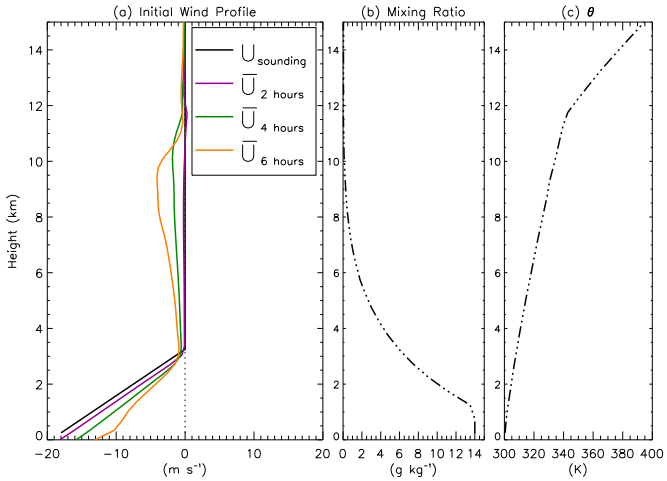

Figure 1. Profiles of (a) zonal wind u (m s^{-1}), (b) mixing ratio q (g kg^{-1}) and (c) potential temperature θ (K) used in the initial sounding for all simulations. Also shown in (a) is the mean wind $\overline{u}$ every two hours for the medium 1 km domain with cyclic boundary conditions.

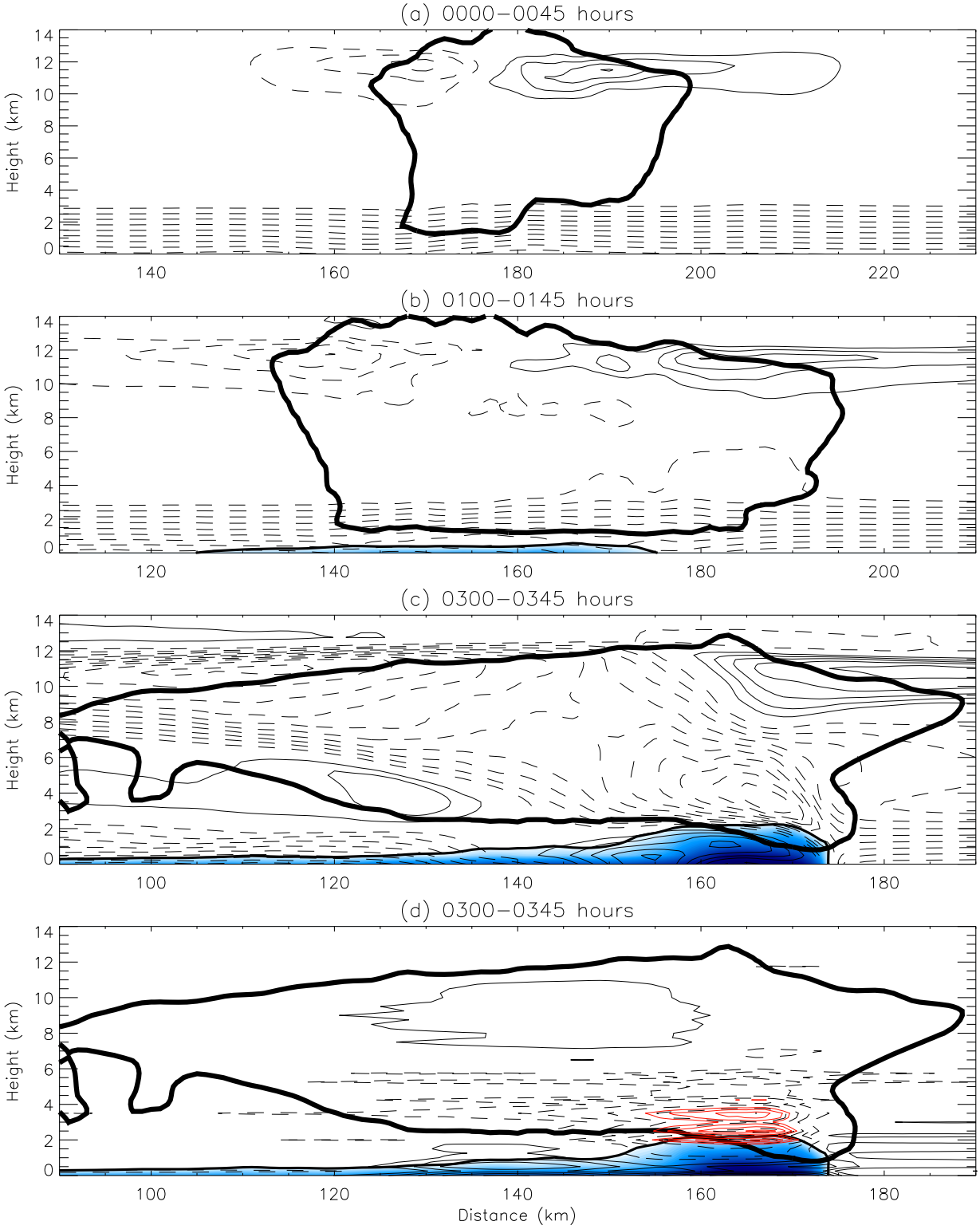

Figure 2. Cross-section of cloud (cloud mixing ratio contour outline 0.1 g kg^{-1} is shown by solid black line) during various stages: (a) 0000-0045 hours, (b) 0100-0145 hours and (c) & (d) 0300-0345 hours when the system is fully developed. (a)-(c) shows contours of u (every 2.0 m s^{-1}, with zero removed) - positive values shown by solid lines and negative by dashed) for medium 1 km resolution cyclic domain. The cold pool is shown by blue shading, using an outer contour of $-1^{\circ}C$ temperature perturbation. (d) The black contours are pressure perturbations every 30 Pa, with negative values shown by dashed lines and positive values shown by solid lines. The red contours shows the pressure perturbations every 30 Pa, less than 150 Pa i.e. the region of lowest pressure.

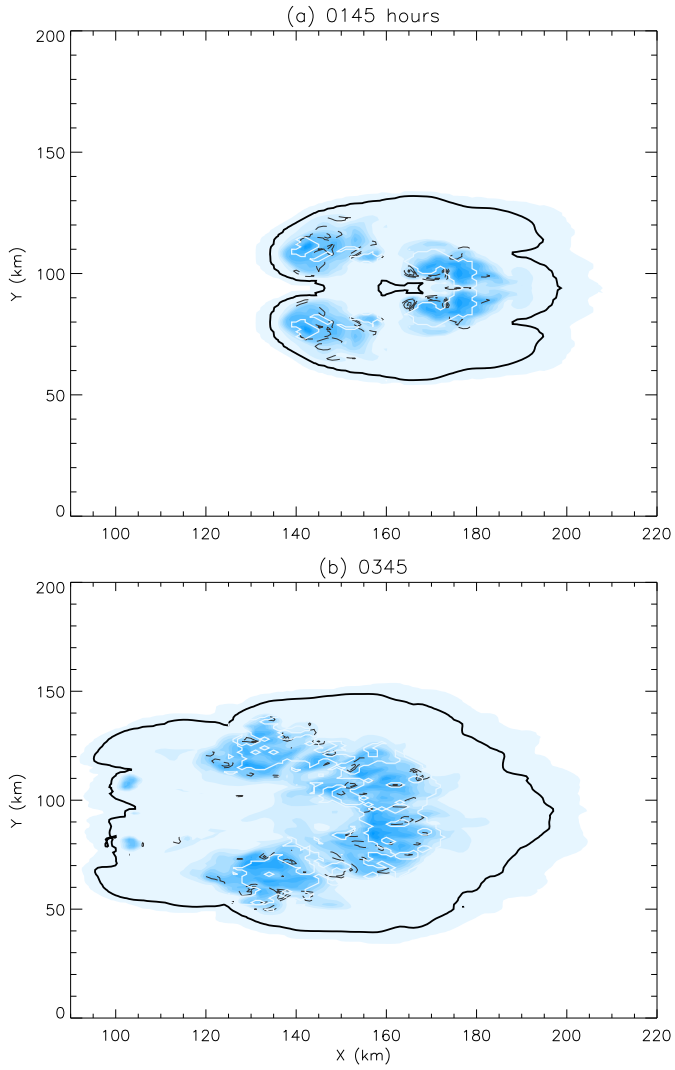

Figure 3. Horizontal cross-section of cloud at 8 km height at (a) 0145 hours and (b) 0300 hours. Cloud outline is cloud mixing ratio 0.1 g kg^{-1}. Black contours represent areas of convective updrafts (defined as in-cloud w $>$ 4 m s^{-1} and 15-min surface rain $>$ 1 mm h^{-1}). The blue shading represents the cloud mixing ratio, the darkest shades represent values of 1.1 g kg^{-1} and the lightest shading is 0.05 g kg^{-1}.

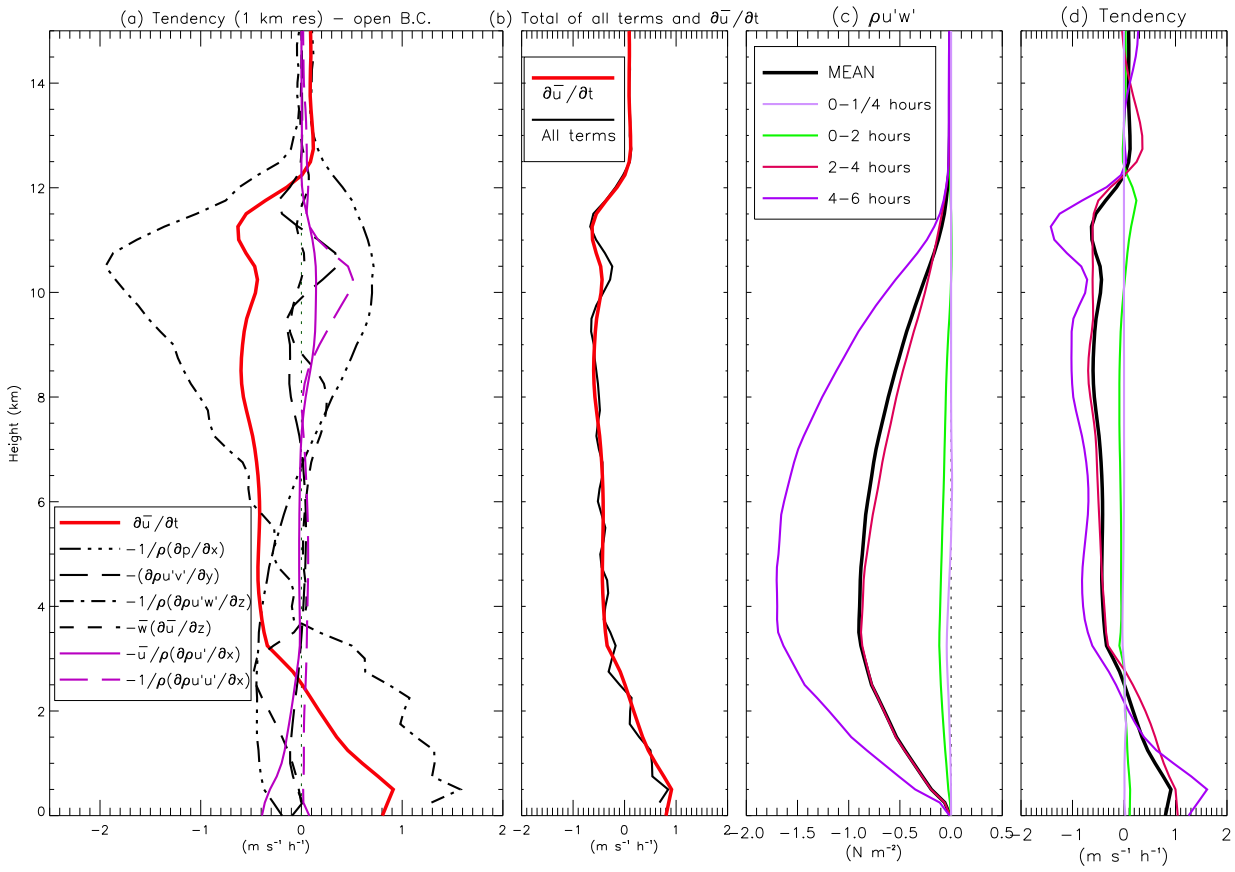

Figure 4. Profiles of (a) the domain mean momentum tendency (red line) and all contributing terms (m s^{-1} h^{-1}) averaged over the 6 h simulation, (b) comparison of the momentum tendency (red line) and the sum of all the terms (black line) (m s^{-1} h^{-1}), (c) momentum transport $\rho u'w'$ (N m^{-2}) and (d) the tendency in m s^{-1} h^{-1} for the 1 km horizontal resolution, medium domain with open boundary conditions. (c) and (d) show various stages throughout the 6 h simulation.

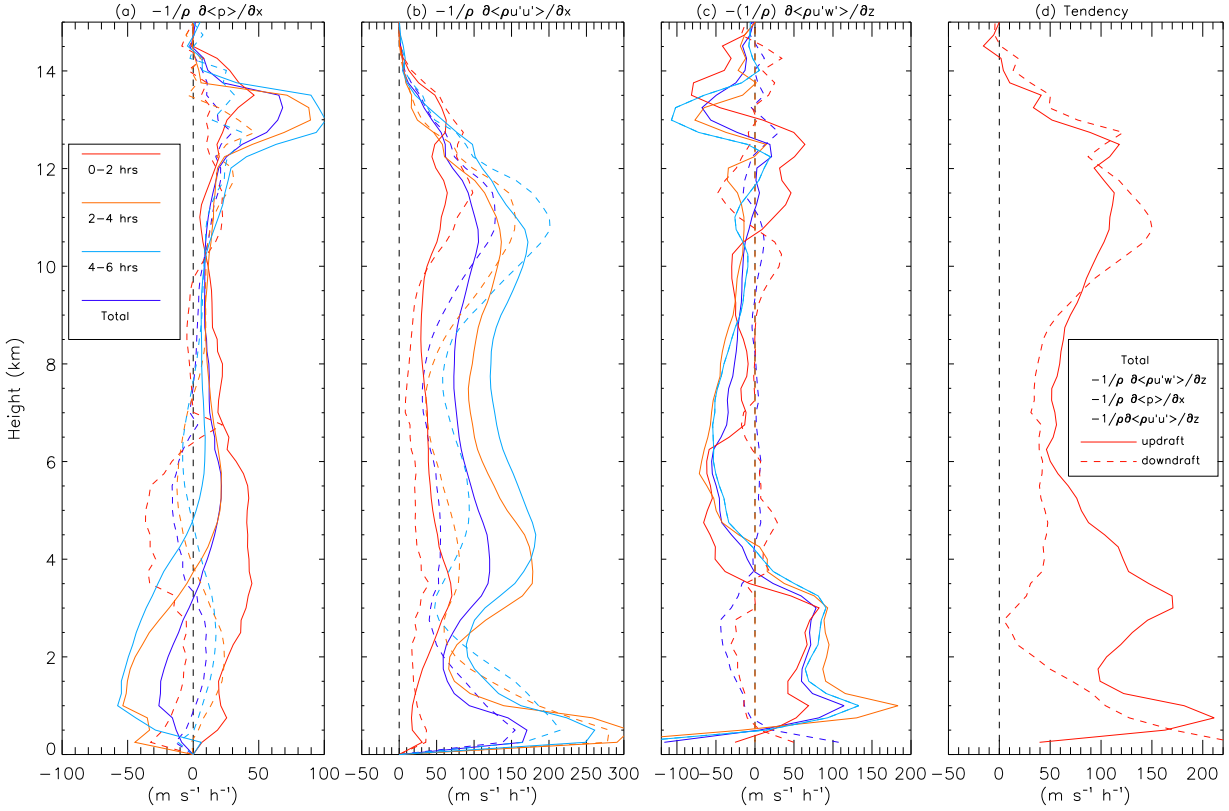

Figure 5. Time-averaged (a) pressure gradients $-\frac{1}{\rho}\frac{\partial p}{\partial x}$ (and area-averaged across the updrafts and downdrafts defined as in-cloud and w $>$ 1 m s^{-1} and $<$ -1 m s $^{-1}$ respectively - represented by $< >$), (b)$-\frac{1}{\rho}\frac{\partial \rho u' u'}{\partial x}$, (c) $-\frac{1}{\rho}\frac{\partial \rho u' w'}{\partial z}$ and (d) the sum of $-\frac{1}{\rho}\frac{\partial \rho u' w'}{\partial z} - \frac{1}{\rho}\frac{\partial p}{\partial x} - \frac{1}{\rho}\frac{\partial \rho u' u'}{\partial x}$ which represents the time-varying tendency, across updrafts for the 1 km horizontal resolution, medium domains with open boundary conditions. Dashed lines are the downdraft profiles and the solid lines are the updrafts.

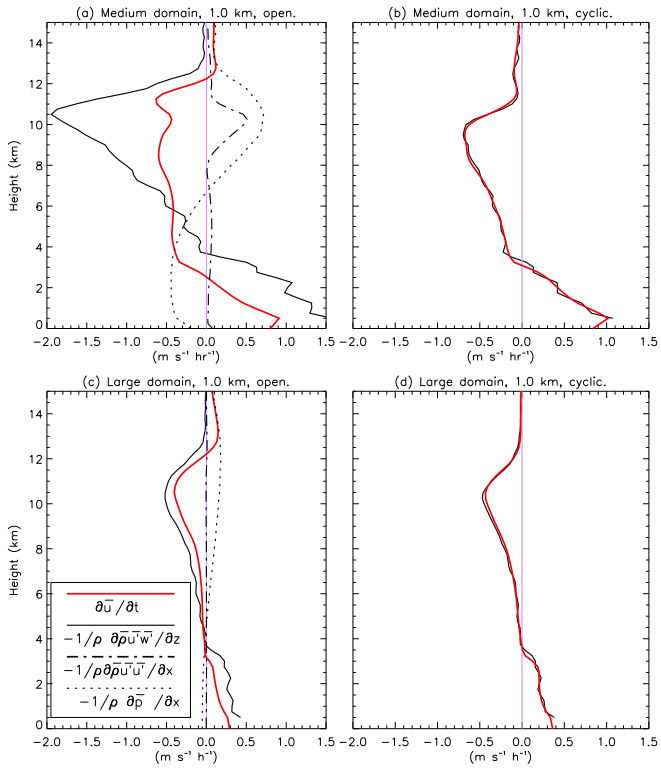

Figure 6. Momentum budgets for 1 km medium (top) and large (below) domains with open (left) and cyclic (right) boundary conditions. The total tendency $\frac{\partial \bar{u}}{\partial t}$ is shown in red.

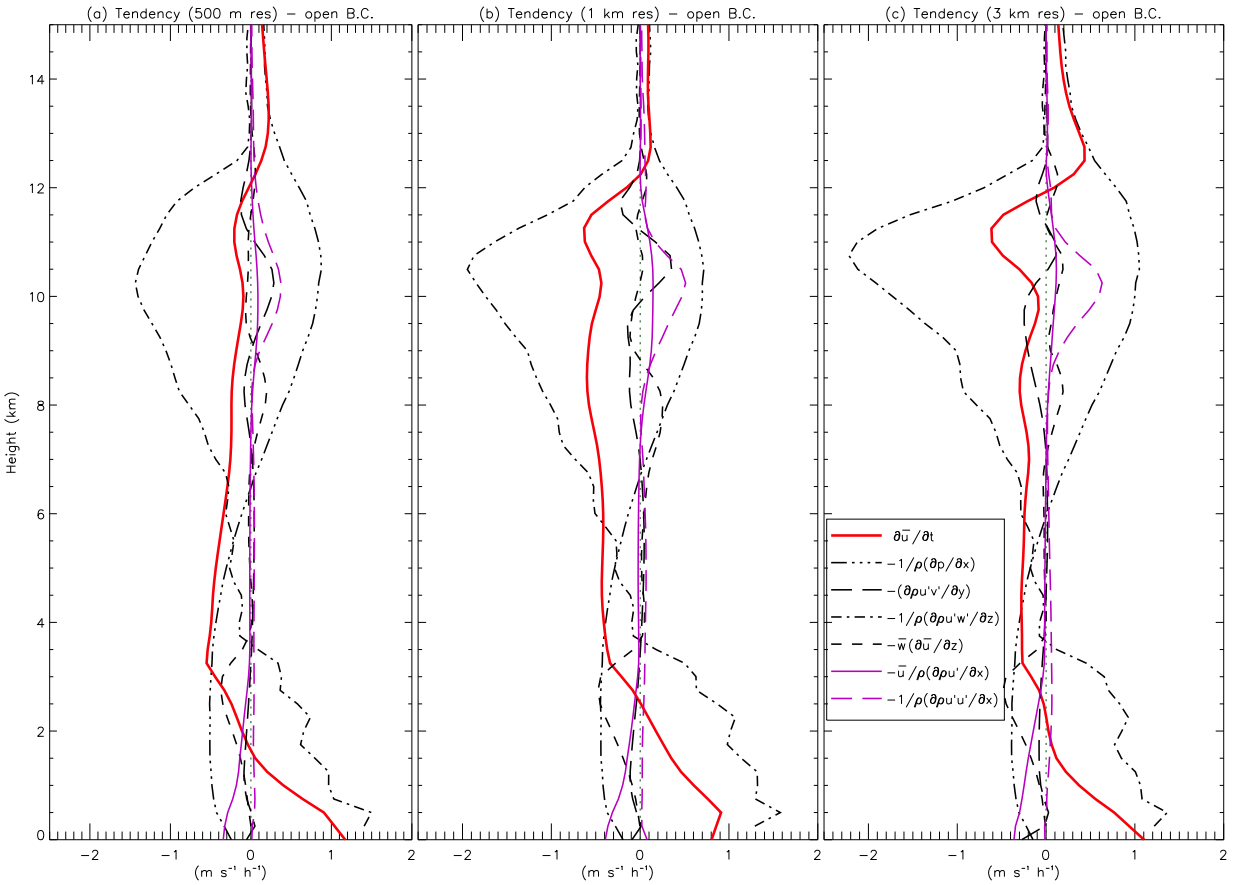

Figure 7. Momentum budget comparison for 500 m (left), 1 km (centre) and 3 km (right) models, for medium domain with open boundaries. Domain average values of terms shown in key.

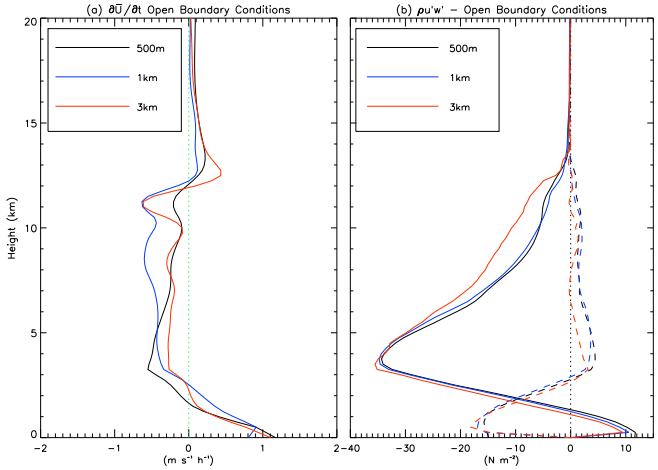

Figure 8. Comparison of the tendency (left) and momentum (right) for open boundary conditions for the various resolution medium domains. The momentum transport contributions of updrafts (solid line) and downdrafts (dashed line) are shown.

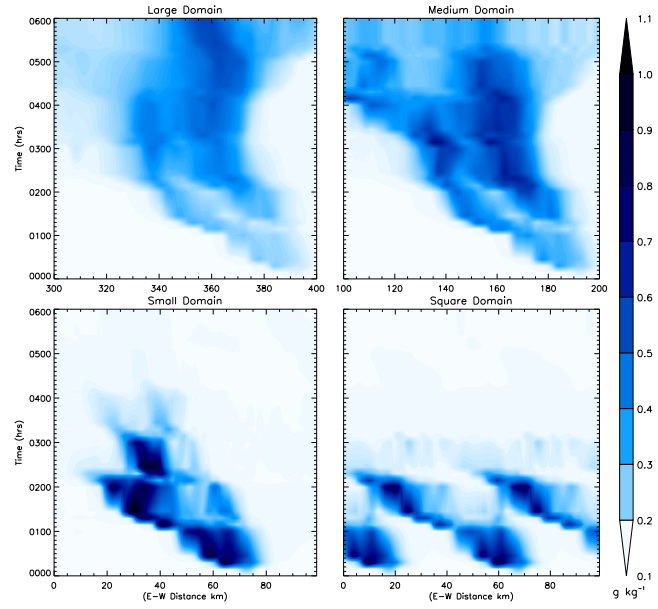

Figure 9. Hovmöller diagrams of cloud for the 1 km cyclic, large and medium domains (top left and right) and small and square domains (below left and right). The square domain was doubled to have the same 100 km width as the other domains (the large and medium domains are trimmed to 100 km). The blue shading shows the average mixing ratio (cloud, rain, ice, snow and graupel) in g kg^{-1}.

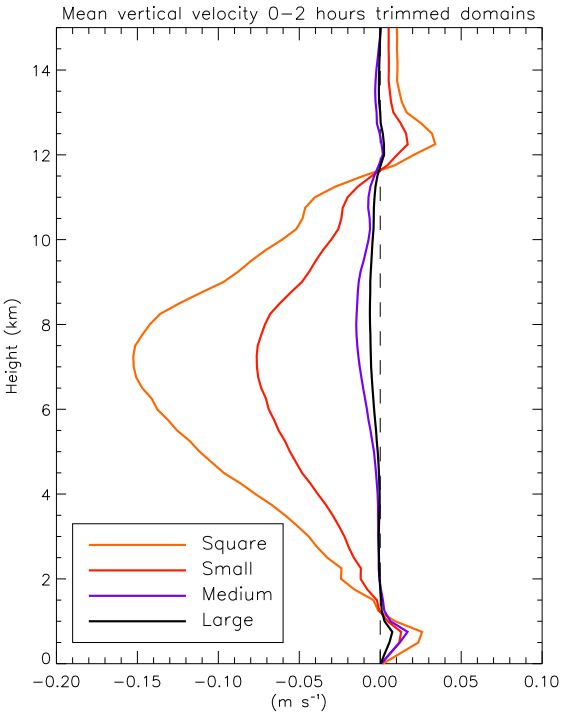

Figure 10. Mean vertical velocity out of cloud across trimmed domains (100 km width) for all cyclic domains at 1 km resolution.

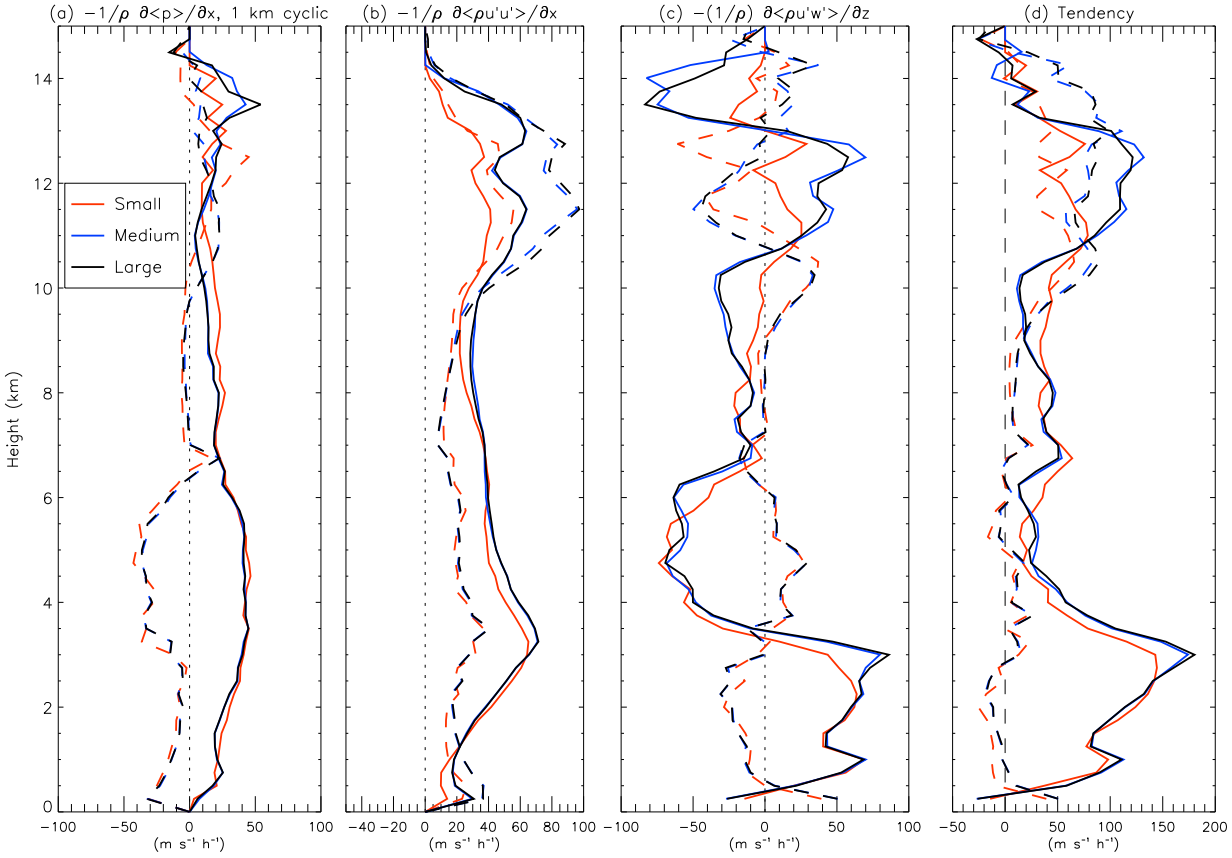

Figure 11. Time-averaged (a) pressure gradients $-\frac{1}{\rho}\frac{\partial p}{\partial x}$, (b)$-\frac{1}{\rho}\frac{\partial \rho u' u'}{\partial x}$, (c) $-\frac{1}{\rho}\frac{\partial \rho u' w'}{\partial z}$ and (d) $-\frac{1}{\rho}\frac{\partial \rho u' w'}{\partial z}$ $-\frac{1}{\rho}\frac{\partial p}{\partial x}$ $-\frac{1}{\rho}\frac{\partial \rho u' u'}{\partial x}$. All terms are averaged across updrafts and downdrafts for the 1 km horizontal resolution domains with cyclic boundary conditions during 0-2 hours (represented by$< >$).

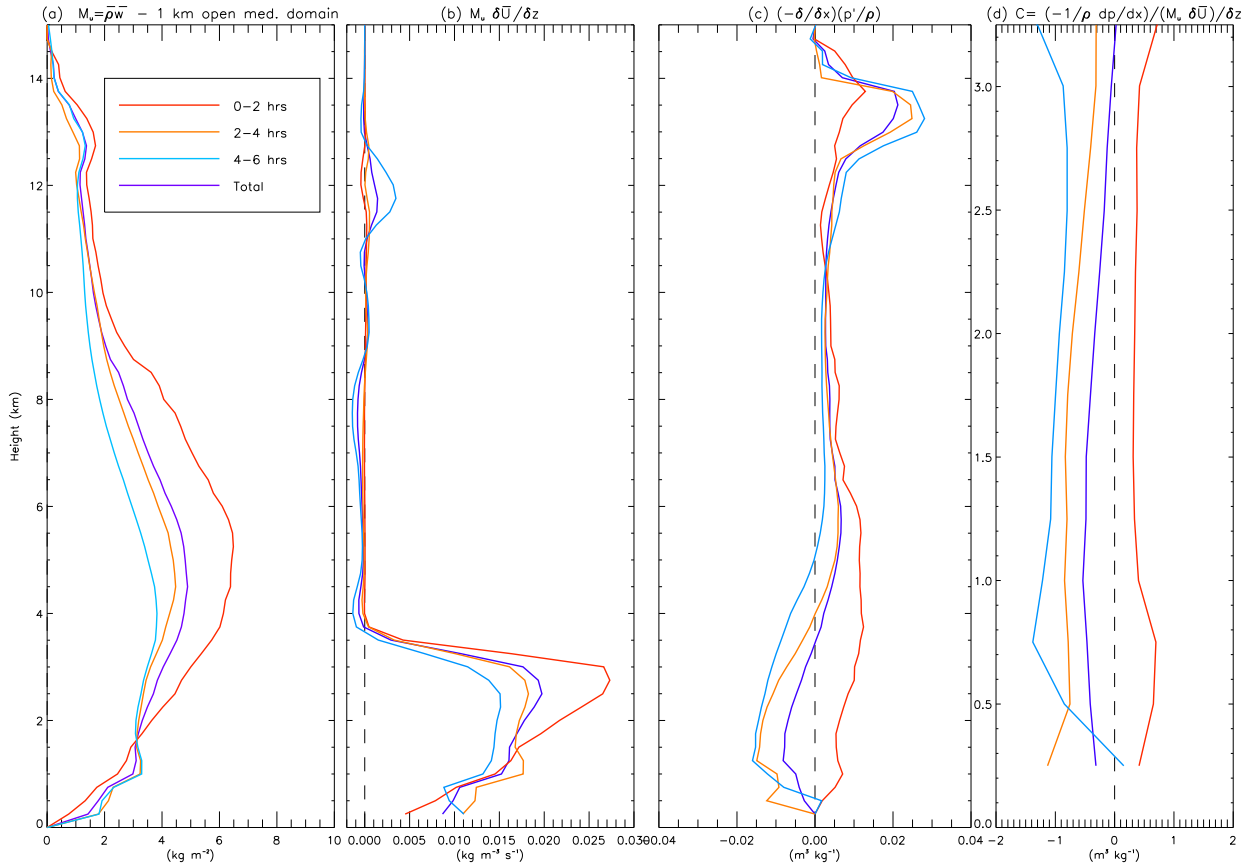

Figure 12. Terms in the relation used in the Gregory parametrisation scheme, $-\frac{\partial}{\partial x}\left(\frac{p}{\rho}\right) \propto C_u M_u \frac{\partial \overline{U}}{\partial z}$ - shows (a) M_u=$\overline{\rho w}$, (b)$M_u \frac{\partial \overline{U}}{\partial z}$, (c) $-\frac{\partial}{\partial x}\frac{p'}{\rho}\Big|_u$ and (d) C_u where $C_u = \frac{-\frac{\partial}{\partial x}\frac{p}{\rho}}{M_u \frac{\partial \overline{u}}{\partial z}}$ but only up to 3.25 km - (the height of the shear level) for the 1 km resolution medium open domain. These terms are averaged across time periods and across updrafts (> 1 m s^{-1}) for each height level.

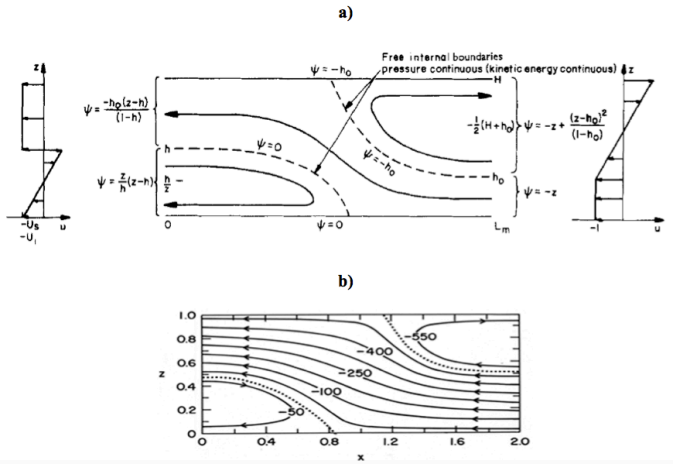

Figure 13. a) Schematic description of the Moncrieff (1992) archetypal model based on the conservation of mass, total energy, vorticity in a Lagrangian framework, and the integral constraint on momentum transport. b) Numerical solution of the two-dimensional vorticity equation shows the characteristic rearward-tilt of the airflow. The dotted and broken lines denote free-boundaries whose shapes are part of the two-dimensional solution, subject to boundary conditions defined by the far-field solution. Fig. a) is from Moncrieff (1992).

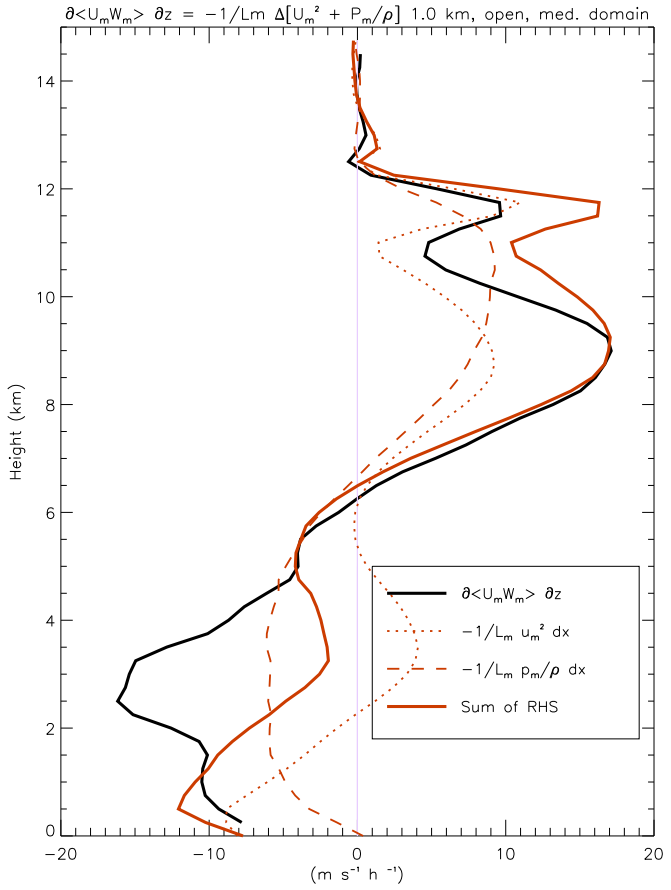

Figure 14. Terms in the relationship $\frac{\partial}{\partial z}\langle u_m w_m\rangle = -\frac{1}{L_m}\Delta\left[u_m^2 + \frac{p_m}{\rho}\right]_0^{L_m}$ for the open lateral boundary conditions for medium domain. Averaged over 0400-0500 hours during the mature stage of evolution. Sum of the terms on the RHS are shown by the solid red line.

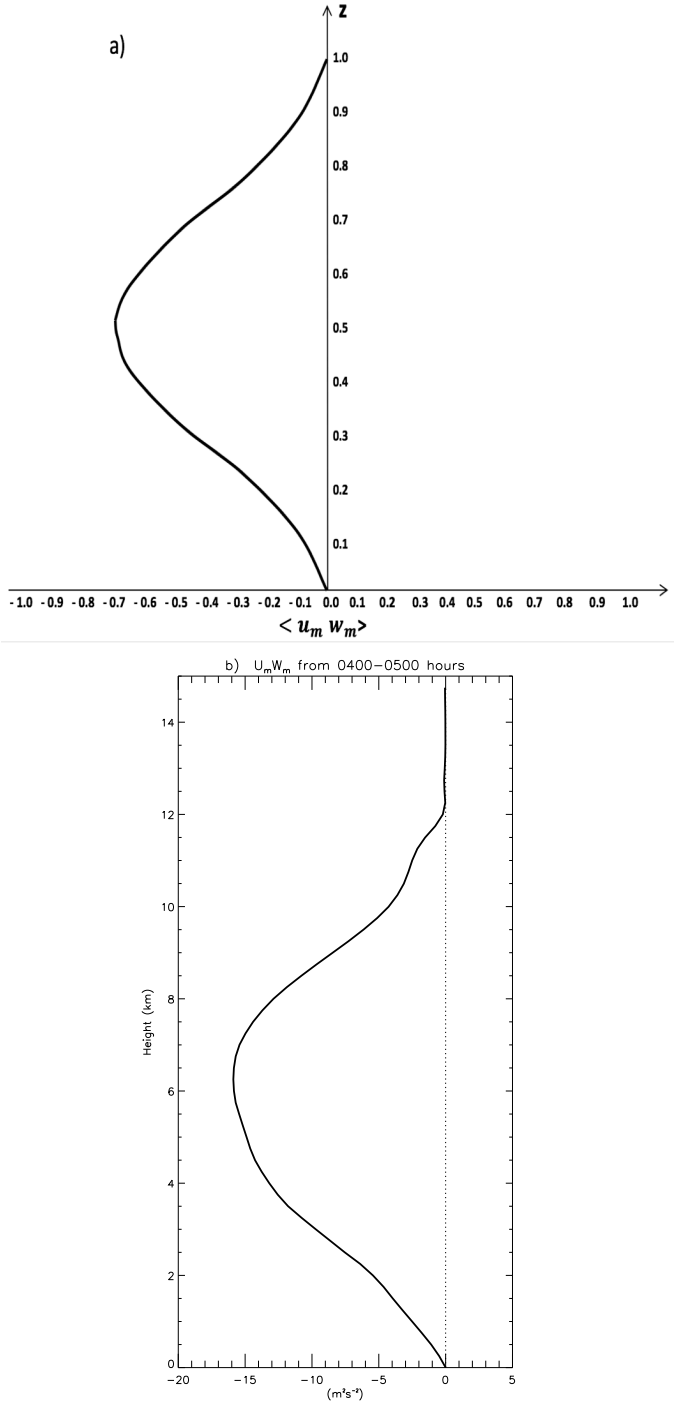

Figure 15. Top - a) Profile of $< u_m w_m >$ for archetypal model in Moncrieff (1992). Below - b) Profile of $u_m w_m$ from the numerical simulation using the medium open domain.